

Supporting Information for

# **Control of Heterogeneous Fe (III) (Hydr)oxide Nucleation and Growth by Interfacial Energies and Local Saturations**

Yandi Hu,<sup>1</sup> Chelsea Neil,<sup>1</sup> Byeongdu Lee,<sup>2</sup> and Young-Shin Jun<sup>1, \*</sup>

<sup>1</sup>*Department of Energy, Environmental & Chemical Engineering,  
Washington University, St. Louis, MO 63130*

<sup>2</sup>*X-ray Science Division, Argonne National Laboratory, Argonne, IL 60439*

*E-mail: [ysjun@seas.wustl.edu](mailto:ysjun@seas.wustl.edu)*

*Phone: (314) 935-4539*

*Fax: (314) 935-7211*

*<http://encl.engineering.wustl.edu/>*

Submitted: March 2013

Revised: July 2013

***Environmental Science & Technology***

## **Summary**

Nineteen pages, including 2 tables and 6 figures.

## Experimental Methods and Data Analysis Details

*Cleaning procedure for single crystal substrates.* Quartz samples and mica sheets were purchased and cut to 1 cm × 1 cm pieces to fit into the GISAXS cell. To remove the surface contaminants, the quartz and mica pieces were sonicated in acetone for 10 minutes. Then, the quartz pieces were further soaked for 1 h in concentrated sulfuric acid (95.0%–98.0%) solution mixed with a commercial oxidizing agent, Nochromix®. Finally, all quartz and mica samples were rinsed with ultrapure water (resistivity > 18.2 MΩ-cm) and stored in micro-filtered distilled water. For corundum, 1 cm × 1 cm square corundum samples with an atomically flat (0001) surface (C-plane) were purchased from MTI Corporation, CA. Each wafer had been packed in a 1000 class clean room using a 100 grade plastic bag with a wafer container. Right before GISAXS measurement, the package was opened and corundum samples were rinsed with ultrapure water (resistivity > 18.2 MΩ-cm). All these heterogeneous Fe(III) (hydr)oxide nucleation and growth experiments were conducted with clean substrates of quartz, mica, and corundum. So initially there is no significant amount of seeds on these substrates for the heterogeneous nucleation and growth, as shown in Figure S2.

*Solution preparation and GISAXS experimental operations.* Solutions were prepared with reagent grade  $\text{Fe}(\text{NO}_3)_3 \cdot 9\text{H}_2\text{O}$ ,  $\text{NaNO}_3$ , and ultrapure water. Right before GISAXS or zeta potential measurements, ultrapure water was added to the weighed salt (0.0452 g  $\text{NaNO}_3$ ) to a final

solution volume of 45 ml and shaken to mix. Then, ultrapure water was added to 0.0202 g  $\text{Fe}(\text{NO}_3)_3 \cdot 9\text{H}_2\text{O}$  to get a final solution volume of 50 ml, which we also quickly shook to mix. Finally, 5 ml of this  $10^{-3}$  M  $\text{Fe}(\text{NO}_3)_3$  solution was added into the 45 ml salt solution and the solution was shaken. The final 50 ml solution contained  $10^{-4}$  M  $\text{Fe}(\text{NO}_3)_3$  and had an ionic strength of 10 mM. Because hydrous Fe(III) oxide precipitation started when the  $10^{-3}$  M  $\text{Fe}(\text{NO}_3)_3$  solution was prepared, timing started from this mixing moment. Only approximately 2 min elapsed before the first GISAXS image was taken. Right at the end of each GISAXS measurements, the solution was removed from the GISAXS cell with a syringe and needle. Then, the substrate surface was quickly rinsed with ultrapure water to remove the residual solution on the surface. After that, the surface was dried in a gentle high purity  $\text{N}_2$  gas stream and stored in boxes for further analyses. *Ex situ* GIWAXS experiments were conducted within 1 day of the GISAXS experiments, and Raman and AFM measurements were conducted within a week. Blank experiments were performed with 10 mM  $\text{NaNO}_3$  without Fe(III), and nothing was observed on the substrate surfaces with either GISAXS or AFM.

***Preparing quartz, mica, and corundum powders in acidic salt solution for zeta potential measurements.*** Quartz, mica, and corundum were ground to powder, and each was separately allowed to settle in an acidic salt solution (10 mM  $\text{NaNO}_3$ , with pH around  $3.7 \pm 0.2$ , adjusted with  $\text{HNO}_3$ ) for 10 min. Then, the upper region of each solution, which contained only small

suspended quartz/mica/corundum powder, was injected into a zeta cell for zeta potential measurements.

***Quartz, mica, and corundum structures.*** Quartz, mica, and corundum crystal structures are shown in Figure S1 using a polyhedral model. The red balls represent oxygen anions. A polyhedron is drawn by using straight lines to connect the oxygen anions, which surround a cation.

Quartz is a framework silicate, which can be described as a network of  $\text{SiO}_4$  tetrahedra, with every corner oxygen of each tetrahedron shared with four adjacent tetrahedra (Figures S1A1 and S1A2).

Muscovite (Figure S1B1) is a sheet silicate, consisting of two tetrahedral (T) Si/Al sheets connected by an Al dioctahedral (O) sheet, forming the so-called T-O-T structures.<sup>1</sup> Due to the isomorphous substitution of the tetravalent silicon by trivalent aluminum in the tetrahedral layer, there is an excess negative surface charge, which is compensated by the interlayer cations, such as  $\text{K}^+$ , shown as the purple balls in Figure 1B1.<sup>1</sup> Cleavage along the (001) plane of muscovite exposes the tetrahedral layer, which is constructed by connected six-member rings, as shown in Figure S1B2.<sup>1</sup>

For corundum ( $\alpha\text{-Al}_2\text{O}_3$ ), which contains  $\text{Al}^{3+}$  and  $\text{O}^{2-}$  ions, the crystal lattice takes the form of a slightly distorted closest hexagonal packing of  $\text{O}^{2-}$  anions, with the  $\text{Al}^{3+}$  cations filling two

thirds of the octahedral sites between the closely packed  $O^{2-}$  anions (Figures S1C1 and S1C2).<sup>2</sup>

The coordination numbers for  $Al^{3+}$  and  $O^{2-}$  are 6 and 4, respectively.<sup>2</sup>

**Nucleation rate.** According to classical nucleation theory (CNT)<sup>3</sup>, for mineral nucleation to occur, a free energy barrier ( $\Delta G^*$ ) must be overcome. The energy barrier originates from the positive contribution of the interfacial free energy to the total free energy change associated with the creation of a crystal precipitate from solution. Taking the nucleation barrier as the activation energy for nucleation to occur, the nucleation rate (I), which is the increase in the number of nuclei per unit volume per unit time, can be described in eqn. S(1), where k is the rate constant:

$$I = k \exp\left(-\frac{\Delta G^*}{RT}\right) cm^{-3} sec^{-1} \quad S(1)$$

During homogeneous nucleation, a solution–precipitate interface is created, and the nucleation energy barrier,  $\Delta G^*_{,homo}$ , as shown in eqn. S(2) and S(3), is a function of the interfacial energy between the precipitates (p) and solution (l),  $\sigma_{pl}$ , and the energy barrier for bulk crystal growth ( $\Delta G_r$ ), which is a function of the saturation of the solution ( $\ln(Q/K) = \ln\Omega$ ).<sup>3</sup> According to eqn. S(1), S(2) and S(3), a higher saturation ( $\Omega$ ) and a lower  $\sigma_{pl}$ , which results in a lower nucleation energy barrier, are preferred for faster homogeneous nucleation.

$$\Delta G^*_{,homo} = \frac{16\pi v^2 \sigma_{pl}^3}{3\Delta G_r^2} \quad S(2)$$

$$\Delta G_r = -RT \ln \Omega \quad S(3)$$

where  $v$  is the molecular volume.

During heterogeneous nucleation, the interfacial free energy originates from the creation of the precipitate ( $p$ )–substrate ( $s$ ) interface and the precipitate ( $p$ )–solution ( $l$ ) interface, as well as the partial covering of the substrate ( $s$ )–solution ( $l$ ) interface, as shown in eqn. S(4):

$$\Delta G_{\text{interface}} = A_{pl}\sigma_{pl} + A_{ps}(\sigma_{ps} - \sigma_{sl}) \quad \text{S(4)}$$

where  $A_{pl}$  and  $A_{ps}$  are the surface areas between the precipitate–liquid and precipitate–substrate interfaces.<sup>3</sup> Considering both the interfacial energy ( $\Delta G_{\text{interface}}$ ) and the energy barrier for bulk crystal growth ( $\Delta G_r$ ), a higher saturation ratio ( $\Omega$ ) and substrate–solution interfacial energy ( $\sigma_{sl}$ ) and a lower precipitate–substrate interfacial energy ( $\sigma_{ps}$ ) are preferred for faster heterogeneous nucleation.

**Growth rate.** There are several different mechanisms for mineral growth: attachment of monomers and polymeric embryos to the preexisting particle, Ostwald ripening, and oriented attachment. During Ostwald ripening, large particles grow at the expense of small particles. If this happened in our system, we would have observed a decrease in the scattering intensity at the high  $q$  range, caused by the dissolution of small particles, because  $q$  is reciprocally related to particle size. This was observed in our previous study of Fe(III) (hydr)oxide precipitation on quartz from NaCl solution.<sup>4</sup> However, this phenomenon was not observed in our current study with  $\text{NaNO}_3$  solution, so we concluded that Ostwald ripening did not occur in our systems within

the 1 h experiments. For oriented attachment, the particles have a preferential alignment direction. If this occurred in our systems, the phenomenon would have been observed by both GISAXS and AFM. However, we did not observe it. Thus, the particle growth in our systems is thought to be caused by the attachment of monomers and polymeric embryos to the preexisting particle, and the particle growth rate is defined as the increase in particle size with time.

**GISAXS scattering curve fitting.** The 1D scattering curves (Figure 1) were fit to eqn. S(5), where  $P(q, R, \sigma)$  is the form factor, and  $S$  is the structure factor.

$$I(q) = I_0 P_0(q, r_0, \sigma_0) S(q, I_{os}, d, R_h, v_f) + I_1 P_1(q, r_1, \sigma_1) \quad S(5)$$

$$P(q, R, \sigma) = (\Delta\rho)^2 \int n(R, \sigma) V^2 \frac{9(\sin(qr) - qR \cos(qR))^2}{(qR)^6} dR \quad S(6)$$

$$S(q, I_{os}, d, R_h, v_f) = I_{os} q^d + S(q, R_h, v_f) \quad S(7)$$

For the form factor  $P(q, r, \sigma)$ , a polydisperse sphere model with the Schultz distribution as a size distribution function was used, as shown in eqn. S(6).  $n(R, \sigma)$  is the Schultz distribution function used to represent the observed size polydispersity of the particles.<sup>5</sup>  $\Delta\rho$  is the electron density difference between the nanoparticles and solutions, and  $V$  is the particle volume. A spherical model was used because when the size distribution is broad and no form factor oscillation is found in the scattering curves, the shape of particles is hard to resolve unless they

are highly anisotropic. Thus, the shape of particles is approximated to a low-resolution, highly symmetric shape, such as a sphere.

The particles showed interparticle distance peaks and power law behavior in the low  $q$  range, which can be modeled by the structure factor,  $S(q, I_{0s}, d, R_h, v_f)$ , as shown in eqn. S(7). The first term,  $I_{0s}q^d$ , models the aggregates, where  $I_{0s}$  is a scaling constant and  $d$  is the Porod power-law exponent for the aggregates.<sup>6</sup> The second term,  $S(q, R_h, v_f)$ , models the local structure in the aggregates. We used the structure factor derived from the hard-sphere Percus-Yevick model, with  $R_h$  and  $v_f$  being the hard-sphere interaction distance and volume fraction, respectively.<sup>7</sup>

**Particle size, volume, and number calculations.** The fitted values of  $R$  and  $\sigma$  after reaction for different times were used to calculate the evolution of the average radii of gyration ( $R_g$ , Figure 2A) of the primary particles, according to the Schultz distribution function.

To calculate the relative total particle volumes (Figure 2B), the fitted intensities ( $I$ ) were used for the integration to calculate the invariant  $Q = \int_0^\infty I(q)q^2 dq$ . In our previous work,<sup>4</sup> Fe(III) precipitation experiments were conducted at the same aqueous condition in the presence of quartz. With 10 times higher X-ray intensity, we were able to observe the  $q$  range from 0.005 to  $0.2 \text{ \AA}^{-1}$  with good signal to noise ratio, and we were able to observe the 1 nm particle (at  $q$  around  $0.05\text{-}0.2 \text{ \AA}^{-1}$ ) formation at later reaction time (after 40 min). In the current study, because



of the much lower X-ray intensity, the signal to noise ratio was low at the high  $q$  range, thus, we were unable to resolve the 1 nm particle clearly. For simplicity, we focused only on the evolution of the initially 2 nm particles, and fittings were conducted over the  $q$  range of 0.005 to 0.08  $\text{\AA}^{-1}$ . Also because of the noise data at high  $q$  range, the invariants were not calculated from the measured data. Considering the perfect agreement between the measured intensities and the fitted curves (Figure 1) over the fitting region, the invariants were calculated from the fitting curve, which can be extended to an infinite  $q$  range based on simulation. In this way, the calculated invariants represent the total volumes of the larger particles grown from 2 to 6 nm ( $V$ , Figure 2B), and did not include the volume of the 1 nm particles. The total particle volumes (Figure 2B) based on invariant calculations were very consistent for the triplicate samples with small error bars. Particle sizes ( $R_g$ , Figure 2A) were calculated based on fitting, and have relatively larger error bars.

Then, assuming a spherical particle shape and using the total particle volumes of the larger particles ( $V$ , Figure 2B) and their average particle sizes ( $R_g$ , Figure 2A), the total particle numbers ( $N$ , Figure 2C) were calculated in relative units:  $N = V/R_g^3$ . The particle sizes on corundum were small (image A); therefore, according to the equation, a small fluctuation in the fitted particle sizes ( $R_g$ ) will cause large fluctuation in particle numbers ( $N$ ) on corundum, as

144 shown in Figure 2C. Even considering this fluctuation, we can conclude that the particle numbers  
145 on corundum were the most among the three substrates (as shown by the guideline in Figure 2C).

146 We also considered the deposition of the homogeneously precipitated particles in solution  
147 onto the substrate surface due to electrostatic interactions or other forces, such as the Van der  
148 Waals force. If the deposition of homogeneously precipitated particles were also a dominant  
149 process for particle formation on the substrate surface as heterogeneous precipitation, we should  
150 have observed particles of two different sizes both abundant on the substrate surface from  
151 GISAXS, as the homogeneously precipitated particles in solution were bigger ( $\sim 10\text{--}20$  nm,  
152 observed by dynamic light scattering, data not shown) than the heterogeneously precipitated  
153 particles. However, based on our GISAXS measurements (Figure 1), we did not observe the 10–  
154 20 nm particles. Thus, there could be a small amount of particles formed in solution being  
155 collected on the substrates, however, their contribution to the total particles observed on the  
156 substrate surfaces was not significant.

## References:

1. Wang, J. W.; Kalinichev, A. G.; Kirkpatrick, R. J.; Cygan, R. T., Structure, energetics, and dynamics of water adsorbed on the muscovite (001) surface: A molecular dynamics simulation. *J. Phys. Chem. B* **2005**, *109*, (33), 15893-15905.
2. Dobrovinskaya, E. R.; Lytvynov, L. A.; Pishchik, V., *Sapphire: material, manufacturing, applications*. Springer: New York, 2009.
3. Lasaga, A. C., *Kinetic theory in the earth sciences*. Princeton University Press: New Jersey, 1998.
4. Hu, Y.; Lee, B.; Bell, C.; Jun, Y.-S., Environmentally abundant anions influence the nucleation, growth, ostwald ripening, and aggregation of hydrous Fe(III) oxides. *Langmuir* **2012**, *28*, (20), 7737-7746.
5. Aragon, S. R.; Pecora, R., Theory of dynamic light scattering from polydisperse systems. *J. Chem. Phys.* **1976**, *64*, (6), 2395-2404.
6. Roe, R. J., *Methods of X-ray and neutron scattering in polymer science*. Oxford University Press: New York, 2000.
7. Kinning, D. J.; Thomas, E. L., Hard-sphere interactions between spherical domains in diblock copolymers. *macromolecules* **1984**, *17*, 1712-1718.
8. Chichagov, A. V., Information-Calculating System on Crystal Structure Data of Minerals (MINCRYST). In *kristallografiya*: 1990; Vol. 35.
9. Xu, W.; Hausner, D. B.; Harrington, R.; Lee, P. L.; Strongin, D. R.; Parise, J. B., structural water in ferrihydrite and constraints this provides on possible structure models. *Am. Mineral.* **2011**, *96*, 513-520.
10. Manceau, A., Critical evaluation of the revised akdalaite model for ferrihydrite. *Am. Mineral.* **2011**, *96*, 521-533.

181 **Table S1** Space groups and lattice parameters of iron (hydr)oxides, quartz, mica, and corundum.<sup>8</sup>

	a (Å)	c (Å)	space group
hematite	5.0380	13.7720	R 3 (-)c
ferrihydrite	5.95	9.06	P63mc
goethite	a = 9.9134, b = 3.0128	c = 4.5800	P nma
lepidocrocite	a = 3.0800, b = 12.5000	c = 3.8700	Cmc2(1)
akaganeite	a = 10.587, b = 3.0311	c = 10.515, Z = 1; $\beta = 90.03^\circ$	I2/m
corundum	4.7540	12.9900	R3(-)c
quartz	4.9137	5.4047	P3(1) 2 1
muscovite	a = 5.1890, b = 8.9960	c = 20.0960, $\beta=95.1800$	C2/c

182

183

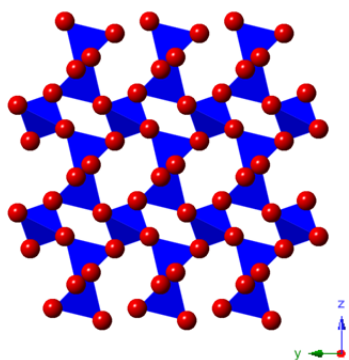
184 **Table S2** Average bond lengths of iron (hydr)oxides, quartz, mica, and corundum.<sup>8-10</sup>

	O–O (Å)	Cation–O (Å)
hematite	2.8	2.0
ferrihydrite	2.8	2.0
goethite	2.8	2.0
lepidocrocite	2.8	2.0
corundum	2.7	1.9
quartz	2.6	1.6
muscovite	2.8	1.6 (Si-O), 1.9 (Al-O)

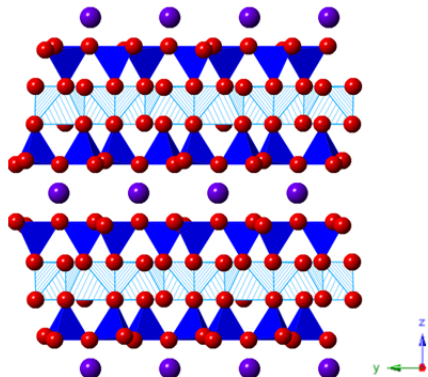
185

186

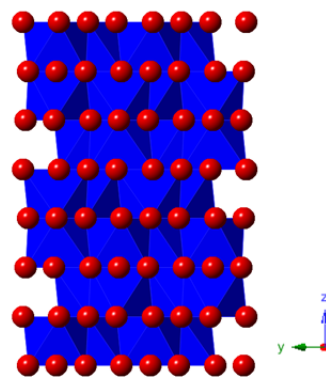
A1. Quartz



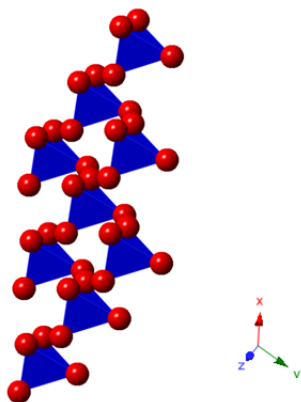
B1. Muscovite



C1. Corundum



A2. Quartz (102) plane



B2. Muscovite (001) plane C2. Corundum (0001) plane

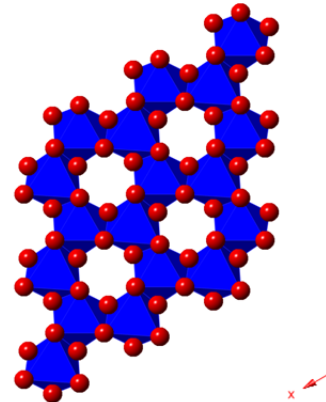
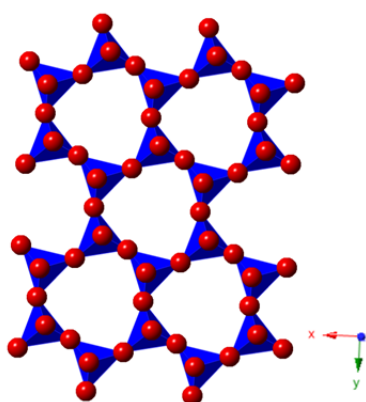


**Figure S1** Polyhedron models of crystal structures for quartz (A), muscovite (B), and corundum (C). The plots were created using Crystal Maker (CrystalMaker®for Windows, version 2.5.2, CrystalMaker Software Ltd.).

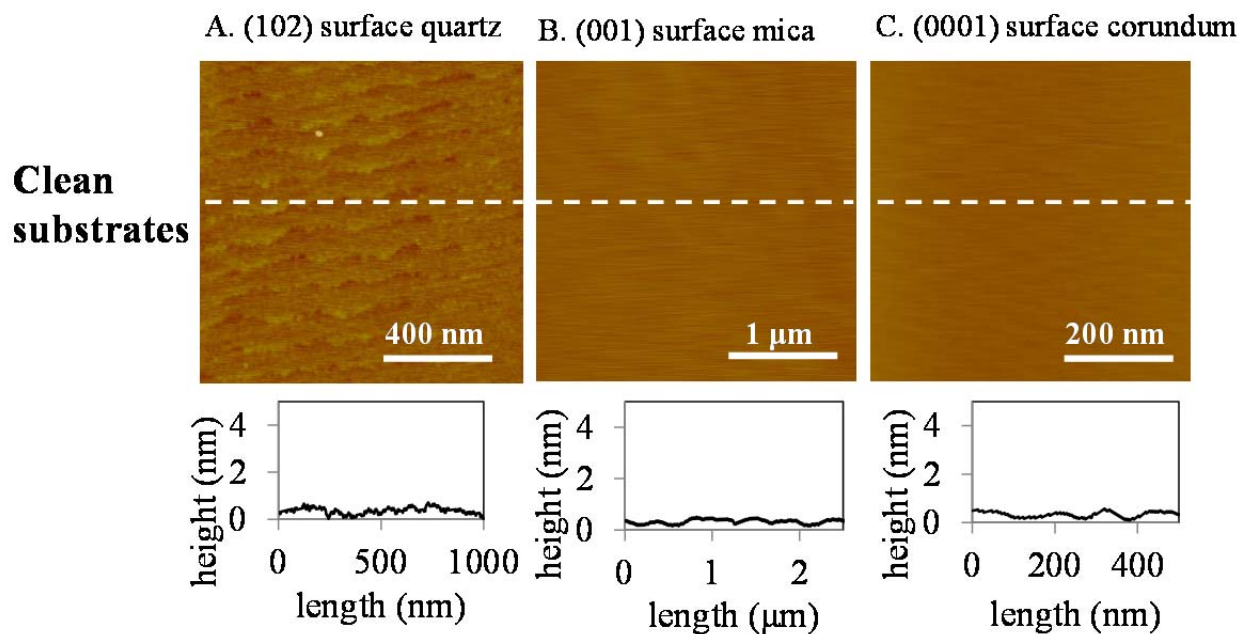


**Figure S2** AFM observations of cleaned quartz (A), mica (B), and corundum(C) surfaces before reactions. The height profiles provided below the images were cut along the dashed white lines.





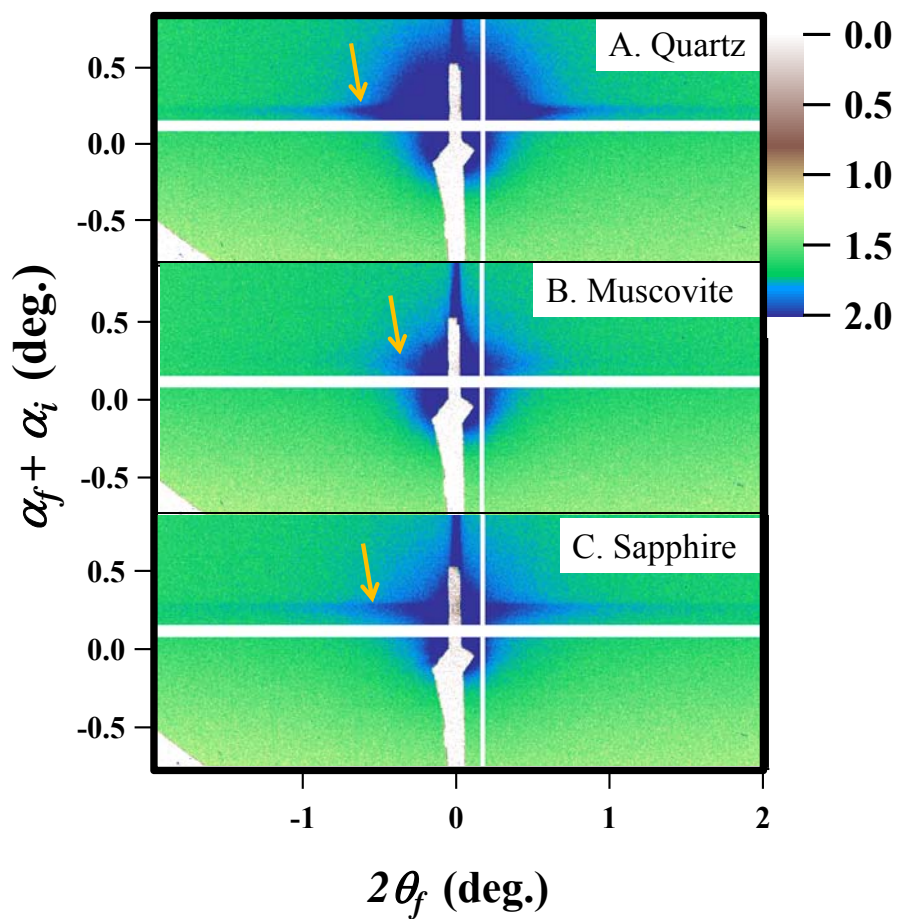
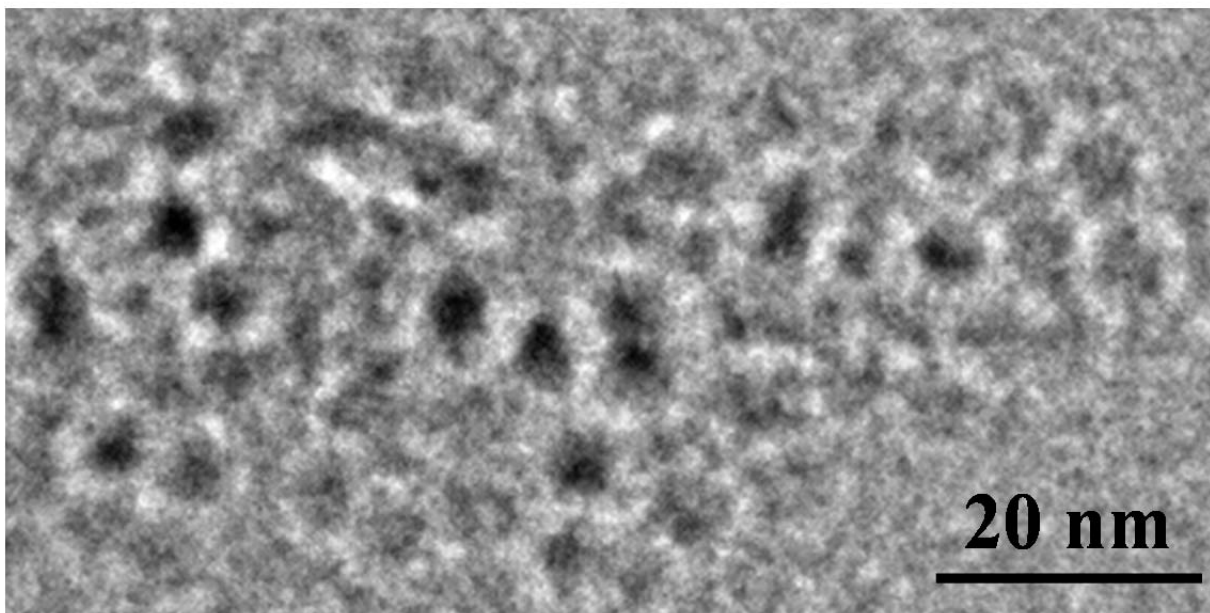


**Figure S4.** 2D images of GISAXS scattering patterns from particles on quartz, mica, and corundum after reaction for half an hour. The orange arrows point at the position of the Yoneda Wing. The white lines in the images are due to a gap between different panels in the 2-dimensional detector.



207

208 **Figure S5.** HRTEM image of particles on a Formvar/carbon-coated Cu grid.

209

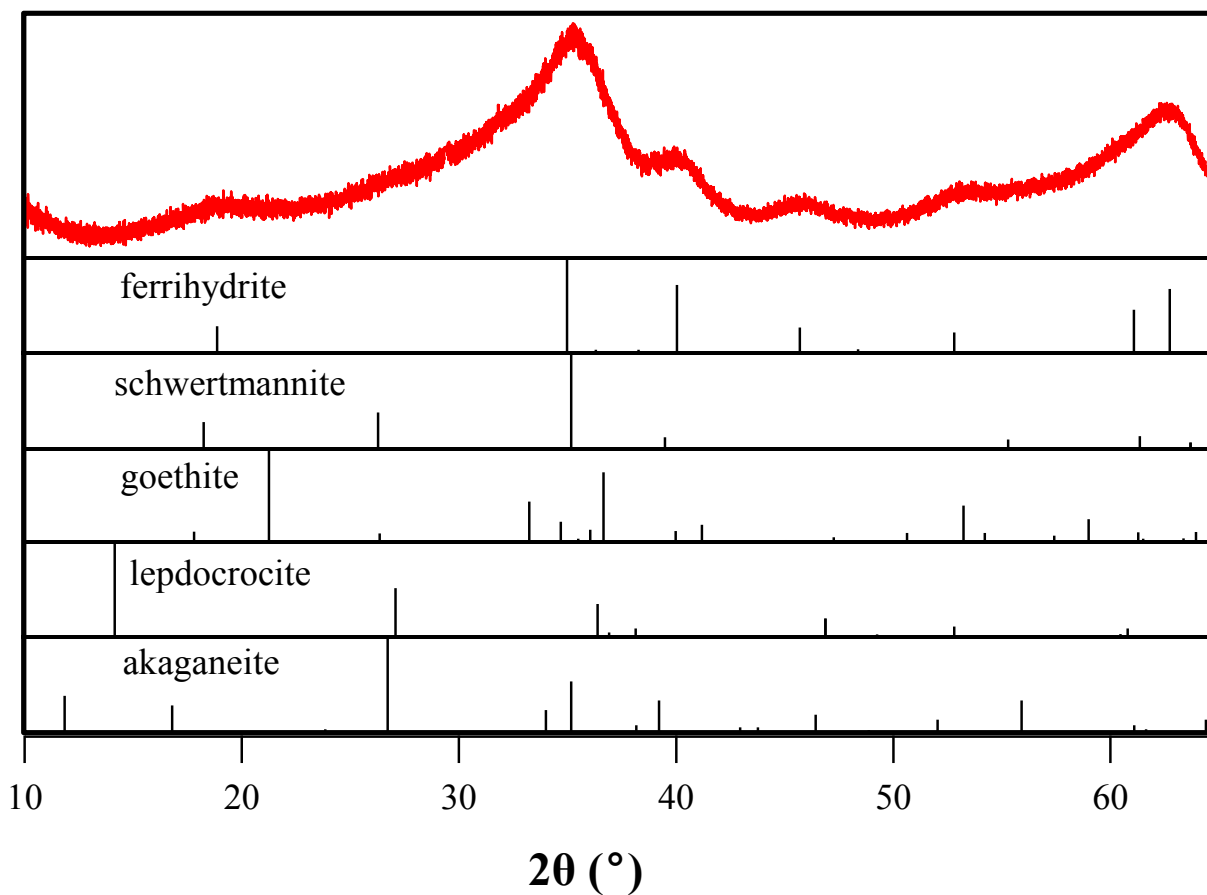


**Figure S6.** HRXRD patterns of the precipitates formed in solution. The XRD peaks of the particles formed match well with the reference of ferrihydrite.